bioRxiv preprint doi: https://doi.org/10.1101/426759; this version posted September 27, 2018. The copyright holder for this preprint (which was not certified by peer review) is the author/funder, who has granted bioRxiv a license to display the preprint in perpetuity. It is made available under aCC-BY-NC-ND 4.0 International license.

High-speed atomic force microscopy visualizes mobility of photosynthetic proteins in grana thylakoid membranes

Bibiana Onoa[1,†,*], Shingo Fukuda[1,†,‡], Masakazu Iwai[2,3], Carlos Bustamante[1,2,4,5,6,7], Krishna K. Niyogi[1,2,3,*]

[1]Howard Hughes Medical Institute, University of California, Berkeley, CA 94720, USA.

[2]Molecular Biophysics and Integrated Bioimaging Division, Lawrence Berkeley National Laboratory, Berkeley, CA 94720, USA.

[3]Department of Plant and Microbial Biology, University of California, Berkeley, CA 94720, USA.

[4]Jason L. Choy Laboratory of Single Molecule Biophysics, University of California, Berkeley, CA 94720, USA.

[5]Department of Molecular and Cell Biology, University of California, Berkeley, CA 94720, USA.

[6]Department of Physics, University of California, Berkeley, CA 94720 USA.

[7]Kavli Energy NanoSciences Institute at the University of California, Berkeley and the Lawrence Berkeley National Laboratory, Berkeley, CA 94720, USA.

***** For correspondence: bibianaonoa@berkeley.edu (BO) and niyogi@berkeley.edu (KKN)

† These authors contributed equally to this work.

Present address: ‡ Nano Life Science Institute (WPI-NanoLSI), Kanazawa University, Kanazawa 920-1192, Japan.

Abstract

Thylakoid membranes in chloroplasts contain photosynthetic protein complexes that convert light energy into chemical energy. Under fluctuating light conditions, photosynthetic protein complexes undergo structural reorganization to maintain photochemical efficiency. However, direct observation of dynamics of photosynthetic complexes in thylakoids remains elusive. Using high-speed atomic force microscopy (HS-AFM), we characterized the mobility of individual protein complexes in grana membranes isolated from *Spinacia oleracea*. We distinguished two different types of membranes according to their protein mobility. A large fraction of membranes contained proteins with quasi-static mobility, following a confined diffusion model. In the remaining fraction, the protein mobility was variable. Both confined and Brownian diffusion models could describe the protein mobility in the latter fraction. The average diffusion coefficient was ~1 $nm^2 s^{-1}$. We also showed direct evidence for rotational protein diffusion in grana membranes. Thus, HS-AFM is powerful to visualize individual photosynthetic complexes and to characterize their dynamics *in situ*.

bioRxiv preprint doi: https://doi.org/10.1101/426759; this version posted September 27, 2018. The copyright holder for this preprint (which was not certified by peer review) is the author/funder, who has granted bioRxiv a license to display the preprint in perpetuity. It is made available under aCC-BY-NC-ND 4.0 International license.

Introduction

Photosynthesis is a fundamental process that sustains virtually all life on earth. Two photosystems (PSI and PSII), the cytochrome b_6f complex (Cyt b_6f), and ATP synthase are the major multisubunit membrane protein complexes that catalyze light-driven chemical reactions to synthesize ATP and NADPH in chloroplast thylakoid membranes (1). Light energy is funneled into the reaction centers of each photosystem through light-harvesting complex (LHC) proteins. LHC proteins of PSII (LHCII) are the most abundant membrane proteins in thylakoid membranes, and they are also known to play an essential role in photoprotection (2-4). Given the complexity of the light reactions of photosynthesis and their regulation, investigation of thylakoid membrane structure and function has long been a central topic in the field of photosynthesis research.

Thylakoid membranes in plant chloroplasts are organized into intricate structures comprised of highly stacked and non-stacked membrane regions called grana and stroma lamellae, respectively (5, 6). It is well established that PSII and LHCII proteins are predominantly localized in grana, whereas PSI and ATP synthase are exclusively located in stroma lamellae (7). Previous studies using electron microscopy (EM) have shown that grana are highly packed with membrane proteins, where PSII and LHCII form a protein supercomplex (8-10). Interestingly, it has been suggested that macroorganization of PSII-LHCII supercomplexes in grana affects the induction of photoprotection, which is also correlated with the diffusion rate of thylakoid membrane proteins (11-13). Thus, photosynthetic membrane proteins are considered to be highly dynamic in thylakoid membranes, which might be vital for optimizing photosynthesis and photoprotection (14). However, the molecular details and dynamics of protein diffusion in the highly crowded grana still remain poorly understood due to the lack of experiments showing both visualization of individual protein complexes and direct measurements of their mobility *in situ*.

To investigate protein diffusion in grana membranes, measurements must be performed in aqueous conditions at biologically relevant temperatures. Atomic force microscopy (AFM) has the potential to achieve such conditions, allowing us to acquire images of biological macromolecules at high spatial resolution (XY < 1 nm and Z < 0.1 nm). AFM has been used to characterize the structure and organization of thylakoid membranes (15-20), and these studies have shown that PSII organization in thylakoid membranes is affected by illumination with different light conditions (16, 18, 19). To achieve higher temporal resolution, high-speed AFM (HS-AFM) was developed (21-25) and successfully used to visualize real-time dynamics of biological macromolecules (see 26, 27 for reviews). However, HS-AFM observation to date has only been successful using *in vitro* samples, such as purified molecules (28-32), proteins in reconstituted lipid bilayers or bacterial membrane preparations (33, 34). Here, we perform HS-AFM observations of grana thylakoid membranes isolated from *Spinacia oleracea*. HS-AFM enabled visualization of dynamic movements of photosynthetic protein complexes *in situ*. Our results indicate that the diffusion behavior of photosynthetic membrane proteins is heterogeneous not only between different grana layers, but also within a single granum. Our HS-AFM experiments indicate that the fraction of mobile membrane

bioRxiv preprint doi: https://doi.org/10.1101/426759; this version posted September 27, 2018. The copyright holder for this preprint (which was not certified by peer review) is the author/funder, who has granted bioRxiv a license to display the preprint in perpetuity. It is made available under aCC-BY-NC-ND 4.0 International license.

proteins is less than 10% of the total population we observed. We postulate that the heterogeneity in protein mobility might have implications in regulatory functions during acclimation mechanisms.

Results

HS-AFM visualizes dimeric photosynthetic complexes without altering macromolecular organization in grana membranes.

We prepared grana membranes from spinach using digitonin as described previously (35) (Fig. S1). We optimized the HS-AFM setup for imaging photosynthetic membrane proteins in grana membranes, such that deflection of the AFM cantilever was detected using a near-infrared laser (830 nm wavelength) to minimize excitation of chlorophylls (see Methods for details). HS-AFM observations indicated that macroorganization of grana membranes and associated protein structures were well preserved (Fig. 1A and Fig. S2). As shown previously (15, 18, 36), grana membranes were highly packed with dimeric complexes with an overall density of ~1456 ± 23 particles/μm^2. The dimeric structures were distributed throughout the membranes, but their structural arrangement appeared to be disordered. A bimodal distribution of height and diameter of the dimeric structures indicated the presence of two populations (Fig. 1B and C), which were previously characterized as PSII (larger diameters and taller structures) and Cyt b_6f (smaller diameters and shorter structures) (17). Immunoblot analysis also confirmed the existence of PSII and Cyt b_6f in our grana membranes prepared using digitonin, which has been shown to keep Cyt b_6f intact in the membranes (17) (Fig. S1). The semi-quantitative structural characterization presented here is insufficient to unambiguously separate these two populations. Specific molecular recognition experiments would be required to do so (e.g. reference 17). It is worth mentioning that modest fluctuations in the dimer's height and size were detected in our time-lapse images which further add uncertainty to dimer assignments. A systematic characterization of this observation will be subject of future work. We also calculated the nearest neighbor distance (NND) distribution function (Fig. 1D). A main peak centered at ~20 nm flanked by shorter (~16 nm) and longer (~25 nm) distances was well fitted, which is also consistent with previous results (18, 37). These results observed by HS-AFM are qualitatively comparable with those observed by conventional AFM performed in air (Figs. S1-2). The protein density and NND distribution observed by HS-AFM are also consistent with those observed by EM (e.g., the samples with no light treatment as shown in refs 36, 38). Taken together, we were able to use HS-AFM to investigate spatiotemporal characteristics of thylakoid protein complexes *in situ* without altering their macroorganization.

HS-AFM revealed heterogeneous protein diffusion in individual grana membranes.

To analyze the dynamics of photosynthetic complexes in grana membranes, we performed HS-AFM observation for 60 s or more per sample. HS-AFM images of representative grana discs are shown in Fig. S2C. We tracked individual protruding dimeric structures to calculate the mean square displacement (MSD, Eq. 1). Based on the

bioRxiv preprint doi: https://doi.org/10.1101/426759; this version posted September 27, 2018. The copyright holder for this preprint (which was not certified by peer review) is the author/funder, who has granted bioRxiv a license to display the preprint in perpetuity. It is made available under aCC-BY-NC-ND 4.0 International license.

level of lateral displacement, grana membranes that we observed here could be divided into two groups. The first group, which comprises approximately 90% of the total grana membranes observed in this study, were termed QSM membranes because they contained dimeric structures with quasi-static mobility (Fig. 2, Movie S1). The distinct dimeric structure of each particle in a QSM membrane was still apparent after averaging 50 frames of the HS-AFM images (Fig. 2A), which indicates that the lateral displacement was confined to a few nanometers. The MSD values of 53 dimeric structures in this representative QSM membrane show that the molecular displacement was less than 10 nm^2 (Fig. 2B). The average MSD trace of all structures (thick line in Fig. 2B) was well fitted to a confined diffusion model (Eq. 2). Because the grana membranes used in this study showed preserved macroorganization (Fig. 1, Figs. S1-2), we consider that the quasi-static mobility observed in the QSM group does not indicate an aberrant state of the membranes. In the second group, which comprises about 10% of the total grana membranes observed in this study, most dimeric structures showed quasi-static mobility and sometimes appeared to be clustered (arrowheads in Fig. S3). However, there was a subpopulation of dimeric structures that displayed larger displacements. Figure 3A shows representative time-lapse HS-AFM images revealing such dimeric structures (see also Movie S2). The individual MSD traces were variable among the selected dimeric structures (thin gray lines), and some of them showed values of up to 100 nm^2 (Fig. 3B). Therefore, the second group of grana membranes was termed VPM for variable protein mobility. The average MSD trace of all observed dimeric structures in the VPM membranes (yellow line in Fig. 3B) fits well to a confined diffusion model (Eq. 2, black dashed line, $R^2 = 0.996$) as compared to a Brownian diffusion model (Eq. 3, orange dotted line, $R^2 = 0.981$). Using Eqs 2 and 4, we obtained the average diffusion coefficient of ~1 $nm^2\ s^{-1}$ that was consistent with previous Monte Carlo simulation reports (see Discussion). This result indicates that, overall, the dimeric structures in the VPM grana membranes still exhibited dynamics that can be explained by a similar diffusion model as those observed in the QSM group.

The average MSD trace of the entire population of particles in the VPM membranes may underestimate a certain subpopulation, which apparently showed an unconfined diffusion. To carefully determine the diffusion of each individual dimeric structure, we first fitted each MSD trace to the confined diffusion model. Next, we extracted each confined domain (L) and correlated it with the diffusion coefficient during the first 4 seconds ($D_{initial}$). We then applied k-means clustering criteria. The results showed that most of the dimeric structures (84%) (Fig. 3C, blue circles) were each confined to a small region (average L = 5.8 ± 0.04 nm). In contrast, the remaining population (Fig. 3C, magenta squares) displayed larger displacements (average L = 44.3 ± 17.6 nm). We re-calculated the average MSD trace separately for these two populations. The average MSD trace (Fig. 3D, blue trace) from the larger population was better fitted to a confined diffusion model (light blue dashed line; Eq. 2, $R^2 = 0.997$) than to a Brownian diffusion model (blue dotted line; Eq. 3 $R^2 = 0.939$). On the other hand, the average MSD trace from the smaller population (Fig. 3D, magenta trace) was well fitted to either a confined (light pink dashed line; Eq. 2, $R^2 = 0.983$) or Brownian diffusion model, (magenta dotted line; Eq. 3, $R^2 = 0.983$). This result illustrates that the diffusion characteristics of this particular population are heterogeneous even within the same VPM grana membrane.

bioRxiv preprint doi: https://doi.org/10.1101/426759; this version posted September 27, 2018. The copyright holder for this preprint (which was not certified by peer review) is the author/funder, who has granted bioRxiv a license to display the preprint in perpetuity. It is made available under aCC-BY-NC-ND 4.0 International license.

It is worth mentioning that we occasionally observed grana membranes that contained larger populations of mobile dimeric structures (>80%) than immobile one (Movie S3). In such cases, dimeric structures tended to collide with each other more frequently, which made it difficult to properly identify individual structures and to track their lateral diffusion. Moreover, the shorter residence time of rapidly diffusing structures was insufficient to accurately measure their dimensions in a given frame (i.e., the structure's size and height appears to fluctuate). That makes it difficult to distinguish whether the mobile dimeric proteins indicate the mobility of PSII, Cyt b_6f, or both.

HS-AFM visualized rotational displacement of dimeric structures in grana

High temporal resolution of HS-AFM in this study also enabled us to analyze rotational displacement of the dimeric structures. In the VPM grana membranes, which contained the dimeric structures with heterogeneous diffusion, we measured changes in the angle (θ) of two adjacent structures during a 1-min observation period (magenta and blue arrows in Fig. 4A; Movie S4). The results indicated that the angle changed from 20 to 80 degrees within a few seconds (Fig. 4B). To further illustrate the rotational diffusion observed here, we calculated a 2D-correlation coefficient of variation (CCV; Eq. 5) of the dimeric structures as shown in Fig. 3A. The dimeric structure showing rotational diffusion exhibited constant fluctuations with an average CCV value of 0.65 throughout the observation (Fig. 4C, red trace). By averaging the total time-lapse images, the dimeric morphology disappeared because of the rotational displacement (red profile, Fig. 4D). In contrast, the other dimeric structure showed an average CCV value of 0.83 (Fig. 4C, blue trace), and the dimeric morphology of this structure stayed the same after averaging the time-lapse images (blue profile in Fig. 4D). It is known that PSII-LHCII supercomplexes in grana can be organized into a higher order of associations (e.g. megacomplexes or two-dimensional crystalline arrays) (39). Intriguingly, it has recently been suggested that there are two types of PSII megacomplexes, in which 80% of the supercomplexes show parallel associations, whereas the other 20% interact in a non-parallel manner with variable associations between the two supercomplexes (40). The rotational displacement of the dimeric structures detected here might indicate the formation of variable associations between PSII-LHCII supercomplexes. Such variable associations between neighboring supercomplexes could be one of the mechanisms causing large organizational changes within the membranes.

Discussion

Our HS-AFM observation revealed the presence of at least two groups of isolated grana membranes according to the diffusion behavior of observed dimeric protein structures. The first group (QSM) represents the majority of grana membranes observed (90% of ~15 grana discs), which contain dimeric structures with quasi-static mobility that fits a confined diffusion model (Fig. 2). The remaining 10% of observed membranes (VPM) contain dimeric structures showing larger displacements and a higher diffusion rate than the first group. The diffusion model for the second group appears to be fitted with both confined and Brownian models, but there are individual trajectories that

bioRxiv preprint doi: https://doi.org/10.1101/426759; this version posted September 27, 2018. The copyright holder for this preprint (which was not certified by peer review) is the author/funder, who has granted bioRxiv a license to display the preprint in perpetuity. It is made available under aCC-BY-NC-ND 4.0 International license.

fit only a Brownian model because of their high diffusion rates (Fig. 3). The architecture and organization of both types of membranes are qualitatively similar (lack of crystalline arrays and similar complex densities). We do not have evidence to suggest the exact reason for this heterogeneity. As we observed a similar density of dimeric structures in both QSM and VPM grana membranes, a possible reason for this heterogeneity could be different lipid compositions in the membranes, which might originate from different parts of thylakoid membranes. Also, it has been previously shown that, in fluctuating light, the organization of PSII-LHCII supercomplexes could undergo reversible transitions from crystalline to fluid phases (18, 36). Therefore, we speculate that the heterogeneous protein mobility observed in this study might partially reflect different physiological conditions or transient events related to photoacclimation mechanisms in the leaves from which the grana were isolated. Future experiments using plants acclimated to different light environments will provide a detailed connection between our HS-AFM observation and physiological mechanisms. In this study, we provide a proof of concept that HS-AFM is a suitable technique to study the protein dynamics in thylakoid membranes.

Molecular confinement is well-described in highly crowded membranes such as thylakoid membranes (41), which would have a significant impact on protein mobility (e.g. diffusion paths and velocities). Fluorescence recovery after photobleaching (FRAP) experiments both in intact or broken chloroplasts and isolated grana membranes have shown that about 80% of chlorophyll-binding proteins are immobile (11, 42). HS-AFM allows us to visualize the displacement of individual dimeric photosynthetic complexes in thylakoid membranes and to characterize their diffusion. Our HS-AFM observation indicated that 90% of observed grana contain immobile proteins, similar to the results reported by FRAP experiments. This suggests that the overall protein immobility in chloroplasts observed by FRAP might reflect the confined protein mobility occurring in grana.

Additionally, our HS-AFM observation revealed that protein diffusion can be segregated even within the same grana disc (Figs. 3, 4). It has been shown by using *in vitro* reconstituted lipid membranes that local protein density is correlated with protein mobility, demonstrating that molecular confinement has an effect on protein diffusion in membranes (33). Unlike such *in vitro* reconstituted lipid membranes, however, we used biological membranes, which contain many different proteins in their native lipid environment. LHCII proteins are most abundant in grana and are suggested to be both immobile and mobile as they can associate with PSII and interact with other LHCII proteins, reorganizing different protein complexes in response to light fluctuations (14). The heterogeneity of protein mobility in a single granum observed here might indicate such different situations of LHCII, some of which are strongly associated with PSII, whereas others diffuse freely between PSII supercomplexes and thereby affect the apparent mobility of dimeric structures. AFM is not able to detect individual LHCII proteins due to their flat, membrane-embedded structures, which do not show a clear protrusion from the membrane surface. To fully understand diffusion of dimeric proteins (PSII and Cyt b_6f) in thylakoid membranes, it will be necessary to consider the effect of these embedded membrane proteins.

bioRxiv preprint doi: https://doi.org/10.1101/426759; this version posted September 27, 2018. The copyright holder for this preprint (which was not certified by peer review) is the author/funder, who has granted bioRxiv a license to display the preprint in perpetuity. It is made available under aCC-BY-NC-ND 4.0 International license.

Our HS-AFM observation indicated that the average diffusion coefficient of dimeric structures in grana is approximately 1 $nm^2 s^{-1}$. The results from FRAP measurements estimated a diffusion coefficient of ~100 $nm^2 s^{-1}$ (42), 100-fold higher than our observation, which is most likely due to the fact that our HS-AFM tracks individual dimeric structures in grana, while FRAP measures the ensemble of chlorophyll-binding proteins. Coarse-grained simulations of individual PSII complexes calculated a diffusion coefficient of 100,000 $nm^2 s^{-1}$ (43). However, this simulation did not account for the molecular crowding effect. Monte Carlo simulations based on FRAP experimental data which include the effect of molecular crowding calculated a diffusion coefficient of 1 $nm^2 s^{-1}$ (37), which agrees well with our direct observation of these complexes. These results emphasize that it is essential for understanding diffusion of membrane proteins to measure not only the mobility of individual molecules but also to consider the effect of molecular crowding (41, 42), which is only achievable experimentally by HS-AFM.

In conclusion, we demonstrate that HS-AFM is a powerful technique for characterizing the dynamics of photosynthetic protein complexes in grana thylakoid membranes. Our real-time HS-AFM observation showed heterogeneous mobility of individual proteins. We also obtained the first direct evidence showing rotational protein diffusion in grana. With our current HS-AFM setup, the molecular displacement of PSII and Cyt b_6f was indistinguishable. Our successful application of HS-AFM to photosynthetic proteins in grana membranes opens a much-needed avenue to address long-standing questions regarding the dynamics of these protein complexes during photoacclimation and photoprotection mechanisms.

Materials and Methods

Grana sample preparation

Grana membranes were prepared from spinach (*Spinacia oleracea*) according to the previous method (35) except for the following modification. Spinach leaves were obtained from a local store and kept in the dark overnight at 4 °C. Digitonin (the final concentration at 0.7% w/v) was used to solubilize chloroplasts (0.4 mg Chl/mL) at 4 °C for 30 min in the buffer containing 50 mM phosphate (pH 7.2), 300 mM sucrose, and 10 mM KCl. Crude grana fractions were removed by centrifugation at 1,000 × g for 3 min at 4 °C. The supernatant was centrifuged at 1,000 × g for 5 min at 4 °C to sediment taller grana. The supernatant was further centrifuged at 1,000 × g for 10 min at 4 °C. The pellet containing shorter-height grana was resuspended in the same buffer and immediately used for AFM observation.

Immunoblot analysis

Membrane samples were solubilized with standard Laemmli sample buffer and separated by electrophoresis using sodium dodecyl sulfate polyacrylamide gel prepared using Any kD TGX precast protein gels (Bio-Rad). Separated proteins in gel were electroblotted onto a polyvinylidene difluoride membrane using Trans-Blot Turbo transfer system according to the manufacturer's instruction (Bio-Rad). Primary antibodies specific for D1 (PSII), PsaD (PSI),

bioRxiv preprint doi: https://doi.org/10.1101/426759; this version posted September 27, 2018. The copyright holder for this preprint (which was not certified by peer review) is the author/funder, who has granted bioRxiv a license to display the preprint in perpetuity. It is made available under aCC-BY-NC-ND 4.0 International license.

Lhcb2 (LHCII), Cyt *f*, and AtpB were obtained commercially (Agrisera) and used according to their recommendations.

Conventional AFM in air

Grana membranes were deposited on freshly cleaved mica in high ionic strength buffer (10 mM Tris-HCl, pH 8.0, 150 mM KCl, and 25 mM $MgCl_2$) (44) and incubated at room temperature for 1–3 h. Mica was rinsed with water ten times and dried under N_2 gas flow for 2 min. We used a Multimode AFM Nanoscope V (Bruker Co.) and performed the observation as described previously (18).

HS-AFM

Grana membranes were diluted 5- to 10-fold in high ionic strength adsorption buffer. Two microliters of the diluted sample was deposited on freshly cleaved mica and incubated for 1 h in the dark. Weakly bound membranes were removed by rinsing 10 times with imaging buffer (10 mM Tris-HCl, pH 8.0, 5 mM $MgCl_2$, 150 mM KCl) followed by a gentle, brief (2 s) puff of high purity Argon gas. The sample was immediately immersed in 2 µL of imaging buffer. For scanning, the HS-AFM bath contained the same imaging buffer. We optimized data acquisition and analyses to deconvolute the noise intrinsic to our HS-AFM (e.g. drift, probe, and scan artifacts) to minimize over-interpretation and maximize unbiased observations. We used the Ando-model HS-AFM (24) equipped with a near-infrared laser (830 nm wavelength) to minimize chlorophyll excitation during observation. All optical components were adjusted to near infrared region except for an objective lens. We used a wide area scanner (maximum range: 6×6 µm^2 in XY-directions and 1 µm in Z-direction). First, we set the scan range between 1×1 µm^2 to 4×4 µm^2 in order to find appropriate membranes. Then, we moved the stage to place the membrane at the cantilever position and observed it with scan range of 150~500 nm^2 at 1 frame s^{-1}. The samples were scanned in liquid using tapping mode at room temperature. The deflection of micron-sized cantilever (AC10DS, Olympus, spring constant ~0.1 N/m, resonance frequency 400~500 kHz in liquid) was detected using an optical beam detector. The free-oscillation amplitude of the cantilever (A_0) was set to ~2 nm, and the set point of feedback amplitude was set to about $0.9A_0$. The detailed procedure of HS-AFM observation was described elsewhere (45).

Data analysis

Individual frames from HS-AFM movies were processed using customized algorithms written in Igor Pro (Wave Metrics Inc). First, noise was reduced by Gaussian filtering followed by a flattening filter to accurately measure heights. Second, entire patches were tracked using a 2D correlation method to correct and minimize lateral drift (29). Finally, the corrected images were aligned to the first frame to remove residual artifactual displacements. Movies whose center of mass from individual frames was satisfactorily aligned were selected for further analysis. Particle dimensions (median heights, diameters, center of mass, etc.) were obtained from those selected by

bioRxiv preprint doi: https://doi.org/10.1101/426759; this version posted September 27, 2018. The copyright holder for this preprint (which was not certified by peer review) is the author/funder, who has granted bioRxiv a license to display the preprint in perpetuity. It is made available under aCC-BY-NC-ND 4.0 International license.

thresholding segmentation (package features) from the particle and pore analysis module included in SPIP™. Dimensional fluctuations and spatial displacements were tracked, plotted, and fit using customized scripts written in Wolfram Mathematica® or Igor Pro. The goodness of fit for normal distributions was done using the Akaike information criterion. The contrast of high resolution images was digitally adjusted to facilitate the visual detection of dimeric structures chosen for particle analysis; therefore, small and membrane-embedded proteins appear invisible. Particle MSD was calculated according to:

$$MSD = \frac{1}{T}\sum(x - x_0)^2 + (y - y_0)^2 \qquad (1)$$

where x and y are the particle's center of mass coordinates at different time points; x_0 and y_0 represents the initial x,y center of mass coordinate; T = total duration of observation. Each MSD trace was then fit with two diffusion models: confined (Eq. 2) (46, 47) and Brownian (Eq. 3).

$$MSD = \frac{L^2}{3}\{1 - e^{-t/\tau}\} + 4D_{macro}t \qquad (2)$$

$$MSD = 4Dt \qquad (3)$$

where D_{macro} = macroscopic diffusion coefficient, L = confined domain, τ = equilibration time, D = the diffusion coefficient of natural diffusion and t = time interval. The microscopic diffusion coefficient (D_{micro}) in the confined diffusion model can be obtained from Eq. 4 (46, 47).

$$D_{micro} = \frac{L^2}{12\tau} \qquad (4)$$

To establish whether or not the particle's diffusion properties were identical, we determined the relationship between L and the initial diffusion coefficient ($D_{initial}$ at ≈ 4 s) or D_{micro} obtained from Eq. 4. We confirmed an apparent particle's segregation from this correlation by applying the k-means clustering criteria. The diffusion coefficients reported in this study were obtained from the best fit (Brownian or confined) to the average trace resulted from each subgroup. The goodness of the fitting was evaluated by determining the squared correlation coefficient R^2.

To dissect the molecular rotational movement, we calculated the correlation coefficient of 2D image (29). After tracking a selected molecule to eliminate lateral diffusion effects, we defined it into a rectangular region of interest (ROI) to calculate the 2D correlation coefficient frame by frame with Eq. 5.

$$CCV = \frac{\sum_m \sum_n (H_{m,n} - \bar{H})(I_{m,n} - \bar{I})}{\sqrt{(\sum_m \sum_n (H_{m,n} - \bar{H})^2)}\sqrt{(\sum_m \sum_n (I_{m,n} - \bar{I})^2)}} \qquad (5)$$

H and I denote the height values at a pixel point (m, n) for the targeted ROI at different time points and the initial one (from the first frame), respectively. $\bar{H}$ and $\bar{I}$ are their respective height mean values of the matrix.

bioRxiv preprint doi: https://doi.org/10.1101/426759; this version posted September 27, 2018. The copyright holder for this preprint (which was not certified by peer review) is the author/funder, who has granted bioRxiv a license to display the preprint in perpetuity. It is made available under aCC-BY-NC-ND 4.0 International license.

Acknowledgments We thank Daniel Westcott and Graham Fleming for critical reading of the manuscript. This work was supported by the U.S. Department of Energy, Office of Science, through the Photosynthetic Systems program in the Office of Basic Energy Sciences. S.F. was supported in part by grant (JP15K21708) from the Ministry of Education, Culture, Sports, Science and Technology (MEXT) of Japan. K.K.N. is an investigator of the Howard Hughes Medical Institute.

Competing interests No competing interests declared.

References

1. Nelson N & Yocum CF (2006) Structure and function of photosystems I and II. *Annu. Rev. Plant Biol.* 57:521-565.
2. Muller P, Li XP, & Niyogi KK (2001) Non-photochemical quenching. A response to excess light energy. *Plant Physiol.* 125(4):1558-1566.
3. Wobbe L, Bassi R, & Kruse O (2016) Multi-level light capture control in plants and green algae. *Trends Plant Sci.* 21(1):55-68.
4. Ruban AV (2016) Nonphotochemical Chlorophyll Fluorescence Quenching: Mechanism and Effectiveness in Protecting Plants from Photodamage. *Plant Physiol* 170(4):1903-1916.
5. Anderson JM (1981) Consequences of spatial separation of photosystem 1 and 2 in thylakoid membranes of higher plant chloroplasts. *FEBS Lett.* 124(1):1-10.
6. Austin JR, 2nd & Staehelin LA (2011) Three-dimensional architecture of grana and stroma thylakoids of higher plants as determined by electron tomography. *Plant Physiol.* 155(4):1601-1611.
7. Andersson B & Anderson JM (1980) Lateral heterogeneity in the distribution of chlorophyll-protein complexes of the thylakoid membranes of spinach chloroplasts. *Biochim. Biophys. Acta* 593(2):427-440.
8. Boekema EJ, van Breemen JF, van Roon H, & Dekker JP (2000) Arrangement of photosystem II supercomplexes in crystalline macrodomains within the thylakoid membrane of green plant chloroplasts. *J. Mol. Biol.* 301(5):1123-1133.
9. Yakushevska AE, *et al.* (2001) Supermolecular organization of photosystem II and its associated light-harvesting antenna in *Arabidopsis thaliana*. *Eur. J. Biochem.* 268(23):6020-6028.
10. Dekker JP, Germano M, van Roon H, & Boekema EJ (2002) Photosystem II solubilizes as a monomer by mild detergent treatment of unstacked thylakoid membranes. *Photosynth Res* 72(2):203-210.
11. Goral TK, *et al.* (2010) Visualizing the mobility and distribution of chlorophyll proteins in higher plant thylakoid membranes: effects of photoinhibition and protein phosphorylation. *Plant J.* 62(6):948-959.
12. Johnson MP, *et al.* (2011) Photoprotective energy dissipation involves the reorganization of photosystem II light-harvesting complexes in the grana membranes of spinach chloroplasts. *Plant Cell* 23(4):1468-1479.

bioRxiv preprint doi: https://doi.org/10.1101/426759; this version posted September 27, 2018. The copyright holder for this preprint (which was not certified by peer review) is the author/funder, who has granted bioRxiv a license to display the preprint in perpetuity. It is made available under aCC-BY-NC-ND 4.0 International license.

13. Goral TK, *et al.* (2012) Light-harvesting antenna composition controls the macrostructure and dynamics of thylakoid membranes in Arabidopsis. *Plant J.* 69(2):289-301.

14. Ruban AV & Johnson MP (2015) Visualizing the dynamic structure of the plant photosynthetic membrane. *Nat Plants* 1:15161.

15. Kirchhoff H, Lenhert S, Buchel C, Chi L, & Nield J (2008) Probing the organization of photosystem II in photosynthetic membranes by atomic force microscopy. *Biochemistry* 47(1):431-440.

16. Sznee K, *et al.* (2011) Jumping mode atomic force microscopy on grana membranes from spinach. *J. Biol. Chem.* 286(45):39164-39171.

17. Johnson MP, Vasilev C, Olsen JD, & Hunter CN (2014) Nanodomains of cytochrome b6f and photosystem II complexes in spinach grana thylakoid membranes. *Plant Cell* 26(7):3051-3061.

18. Onoa B, *et al.* (2014) Atomic force microscopy of photosystem II and its unit cell clustering quantitatively delineate the mesoscale variability in Arabidopsis thylakoids. *PLoS One* 9(7):e101470.

19. Stoichev S, *et al.* (2015) Low pH modulates the macroorganization and thermal stability of PSII supercomplexes in grana membranes. *Biophys. J.* 108(4):844-853.

20. Phuthong W, *et al.* (2015) The use of contact mode atomic force microscopy in aqueous medium for structural analysis of spinach photosynthetic complexes. *Plant Physiol.* 169(2):1318-1332.

21. Kodera N, Yamashita H, & Ando T (2005) Active damping of the scanner for high-speed atomic force microscopy. *Rev. Sci. Instrum.* 76(5).

22. Kodera N, Sakashita M, & Ando T (2006) Dynamic proportional-integral-differential controller for high-speed atomic force microscopy. *Rev. Sci. Instrum.* 77(8).

23. Fantner GE, *et al.* (2006) Components for high speed atomic force microscopy. *Ultramicroscopy* 106(8-9):881-887.

24. Ando T, Uchihashi T, & Fukuma T (2008) High-speed atomic force microscopy for nano-visualization of dynamic biomolecular processes. *Prog Surf Sci* 83(7-9):337-437.

25. Fukuda S, *et al.* (2013) High-speed atomic force microscope combined with single-molecule fluorescence microscope. *Rev. Sci. Instrum.* 84(7):073706.

26. Ando T, Uchihashi T, & Scheuring S (2014) Filming biomolecular processes by high-speed atomic force microscopy. *Chem Rev* 114(6):3120-3188.

27. Rajendran A, Endo M, & Sugiyama H (2014) State-of-the-art high-speed atomic force microscopy for investigation of single-molecular dynamics of proteins. *Chem. Rev.* 114(2):1493-1520.

28. Kodera N, Yamamoto D, Ishikawa R, & Ando T (2010) Video imaging of walking myosin V by high-speed atomic force microscopy. *Nature* 468(7320):72-76.

29. Uchihashi T, Iino R, Ando T, & Noji H (2011) High-speed atomic force microscopy reveals rotary catalysis of rotorless F(1)-ATPase. *Science* 333(6043):755-758.

bioRxiv preprint doi: https://doi.org/10.1101/426759; this version posted September 27, 2018. The copyright holder for this preprint (which was not certified by peer review) is the author/funder, who has granted bioRxiv a license to display the preprint in perpetuity. It is made available under aCC-BY-NC-ND 4.0 International license.

30. Miyagi A, Ando T, & Lyubchenko YL (2011) Dynamics of nucleosomes assessed with time-lapse high-speed atomic force microscopy. *Biochemistry* 50(37):7901-7908.

31. Suzuki Y, Shin M, Yoshida A, Yoshimura SH, & Takeyasu K (2012) Fast microscopical dissection of action scenes played by Escherichia coli RNA polymerase. *FEBS Lett.* 586(19):3187-3192.

32. Katan AJ, Vlijm R, Lusser A, & Dekker C (2015) Dynamics of nucleosomal structures measured by high-speed atomic force microscopy. *Small* 11(8):976-984.

33. Casuso I, *et al.* (2012) Characterization of the motion of membrane proteins using high-speed atomic force microscopy. *Nat Nanotechnol* 7(8):525-529.

34. Ruan Y, *et al.* (2017) Direct visualization of glutamate transporter elevator mechanism by high-speed AFM. *Proc. Natl. Acad. Sci. U. S. A.* 114(7):1584-1588.

35. Anderson JM & Boardman NK (1966) Fractionation of the photochemical systems of photosynthesis. I. Chlorophyll contents and photochemical activities of particles isolated from spinach chloroplasts. *Bibl Laeger* 112(3):403-421.

36. Kouril R, Wientjes E, Bultema JB, Croce R, & Boekema EJ (2013) High-light vs. low-light: effect of light acclimation on photosystem II composition and organization in Arabidopsis thaliana. *Biochim Biophys Acta* 1827(3):411-419.

37. Kirchhoff H, Tremmel I, Haase W, & Kubitscheck U (2004) Supramolecular photosystem II organization in grana thylakoid membranes: evidence for a structured arrangement. *Biochemistry* 43(28):9204-9213.

38. Betterle N, *et al.* (2009) Light-induced dissociation of an antenna hetero-oligomer is needed for non-photochemical quenching induction. *J. Biol. Chem.* 284(22):15255-15266.

39. Dekker JP & Boekema EJ (2005) Supramolecular organization of thylakoid membrane proteins in green plants. *Biochim. Biophys. Acta* 1706(1-2):12-39.

40. Nosek L, Semchonok D, Boekema EJ, Ilik P, & Kouril R (2017) Structural variability of plant photosystem II megacomplexes in thylakoid membranes. *Plant J* 89(1):104-111.

41. Kirchhoff H (2014) Diffusion of molecules and macromolecules in thylakoid membranes. *Biochim Biophys Acta* 1837(4):495-502.

42. Kirchhoff H, Haferkamp S, Allen JF, Epstein DB, & Mullineaux CW (2008) Protein diffusion and macromolecular crowding in thylakoid membranes. *Plant Physiol* 146(4):1571-1578.

43. van Eerden FJ, *et al.* (2017) Molecular Dynamics of Photosystem II Embedded in the Thylakoid Membrane. *J Phys Chem B* 121(15):3237-3249.

44. Scheuring S, *et al.* (2004) Watching the photosynthetic apparatus in native membranes. *Proc. Natl. Acad. Sci. U. S. A.* 101(31):11293-11297.

45. Uchihashi T, Kodera N, & Ando T (2012) Guide to video recording of structure dynamics and dynamic processes of proteins by high-speed atomic force microscopy. *Nat. Protoc.* 7(6):1193-1206.

bioRxiv preprint doi: https://doi.org/10.1101/426759; this version posted September 27, 2018. The copyright holder for this preprint (which was not certified by peer review) is the author/funder, who has granted bioRxiv a license to display the preprint in perpetuity. It is made available under aCC-BY-NC-ND 4.0 International license.

46. Ishihama Y & Funatsu T (2009) Single molecule tracking of quantum dot-labeled mRNAs in a cell nucleus. *Biochem. Biophys. Res. Commun.* 381(1):33-38.

47. Daumas F, *et al.* (2003) Confined diffusion without fences of a G-protein-coupled receptor as revealed by single particle tracking. *Biophys. J.* 84(1):356-366.

bioRxiv preprint doi: https://doi.org/10.1101/426759; this version posted September 27, 2018. The copyright holder for this preprint (which was not certified by peer review) is the author/funder, who has granted bioRxiv a license to display the preprint in perpetuity. It is made available under aCC-BY-NC-ND 4.0 International license.

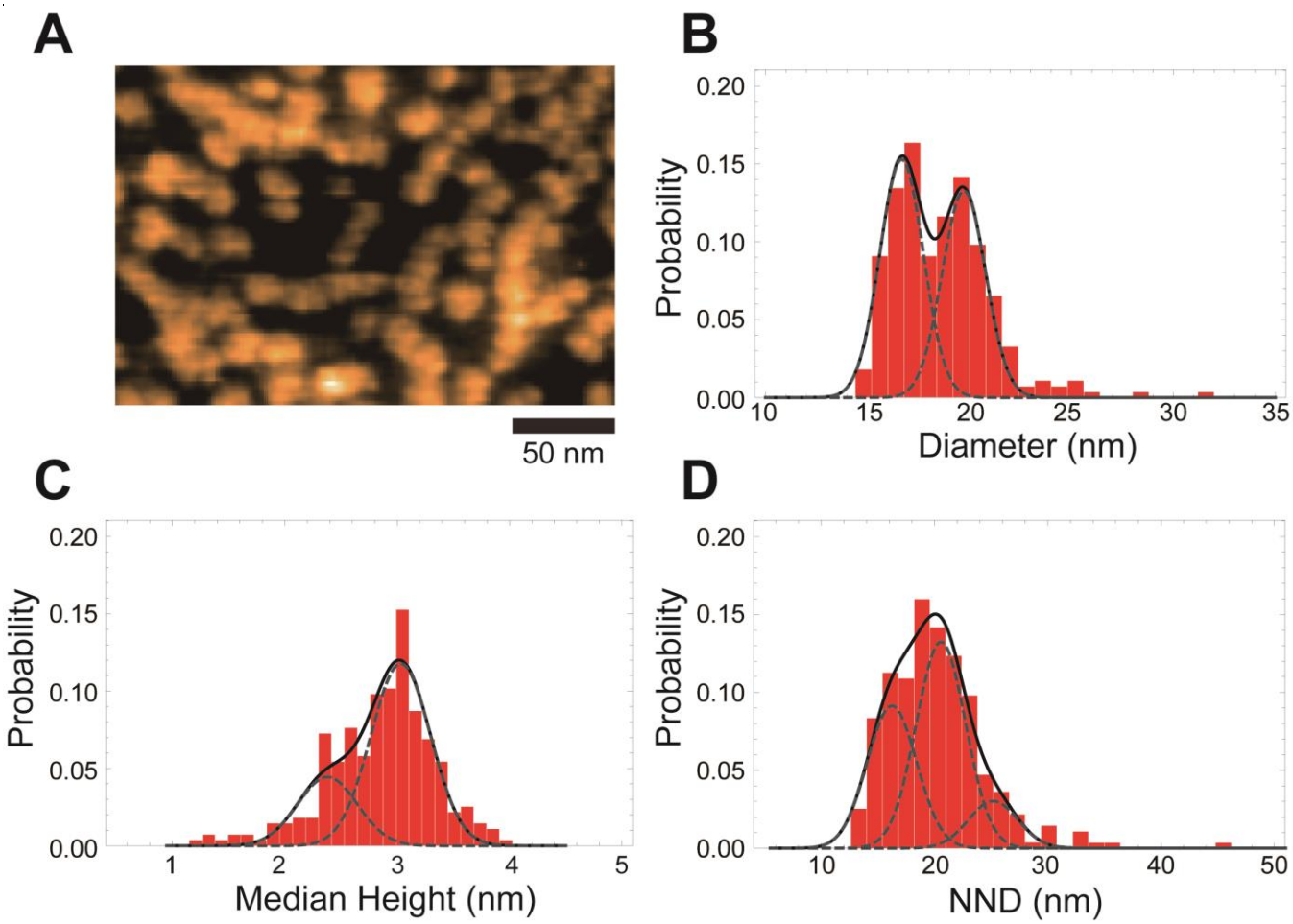

Figure 1

bioRxiv preprint doi: https://doi.org/10.1101/426759; this version posted September 27, 2018. The copyright holder for this preprint (which was not certified by peer review) is the author/funder, who has granted bioRxiv a license to display the preprint in perpetuity. It is made available under aCC-BY-NC-ND 4.0 International license.

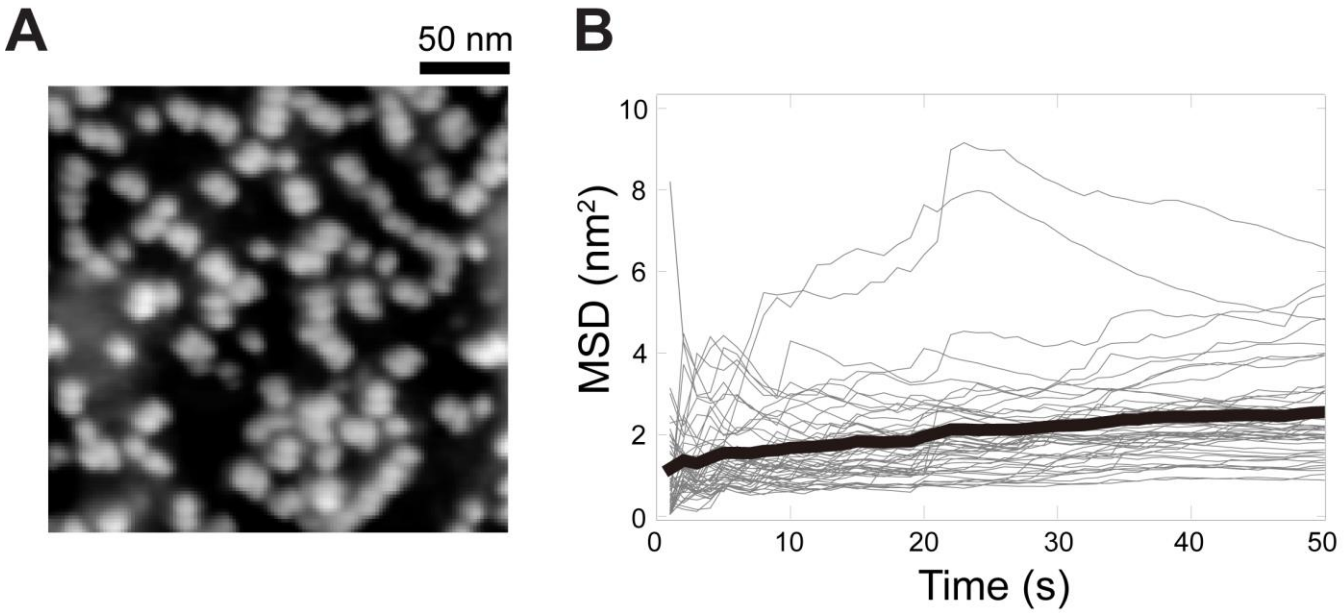

Figure 2

bioRxiv preprint doi: https://doi.org/10.1101/426759; this version posted September 27, 2018. The copyright holder for this preprint (which was not certified by peer review) is the author/funder, who has granted bioRxiv a license to display the preprint in perpetuity. It is made available under aCC-BY-NC-ND 4.0 International license.

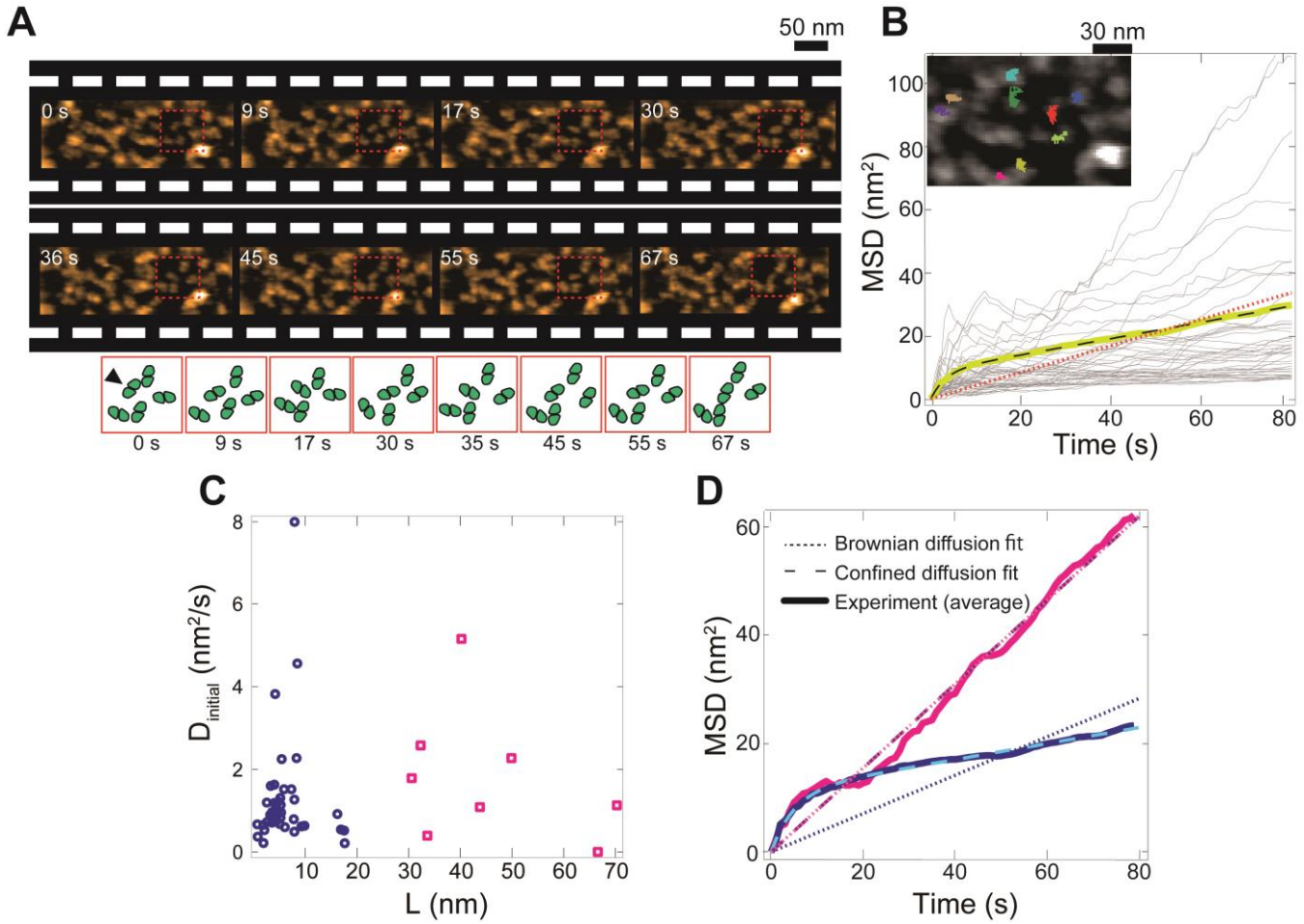

Figure 3

bioRxiv preprint doi: https://doi.org/10.1101/426759; this version posted September 27, 2018. The copyright holder for this preprint (which was not certified by peer review) is the author/funder, who has granted bioRxiv a license to display the preprint in perpetuity. It is made available under aCC-BY-NC-ND 4.0 International license.

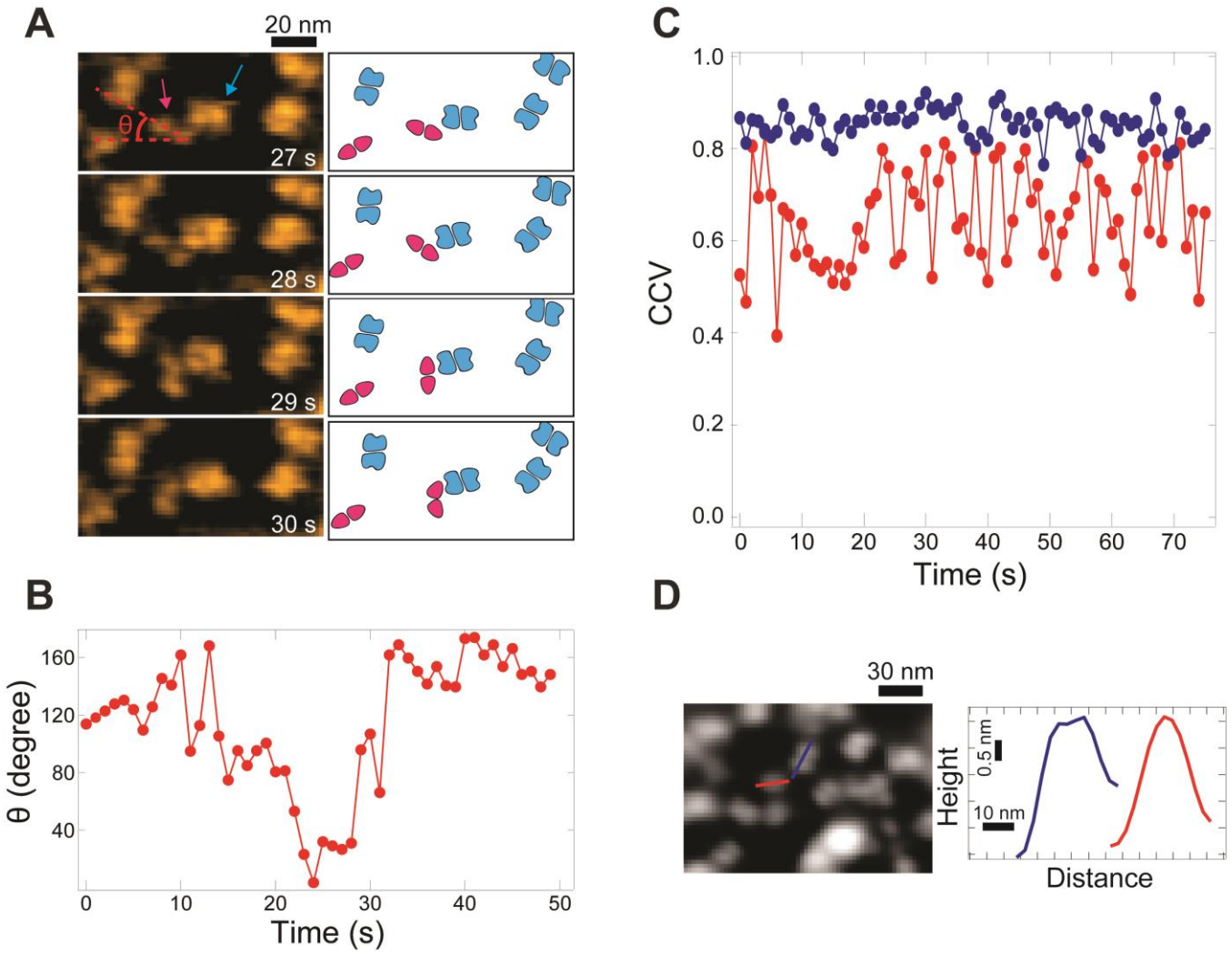

Figure 4

bioRxiv preprint doi: https://doi.org/10.1101/426759; this version posted September 27, 2018. The copyright holder for this preprint (which was not certified by peer review) is the author/funder, who has granted bioRxiv a license to display the preprint in perpetuity. It is made available under aCC-BY-NC-ND 4.0 International license.

Figure legends

Figure 1. HS-AFM characterization of the dimeric protein structures in grana. (**A**) Micrograph of a grana membrane taken from a representative HS-AFM movie. Z-scale, 6.0 nm. The contrast of the membrane was adjusted to enhance the dimeric structures; small, membrane-embedded proteins such as LHCII are invisible. (**B-D**) Probability distribution of diameter（B), median height (C) and nearest neighbor distance (NND) (D) of dimeric structures (N = 275) selected from five different grana thylakoid membranes. Protein selection was limited to those with diameter ≥ 15 nm (70%). The distributions were fitted with double (diameter and height) and three (NND) Gaussians. The goodness of fitting was evaluated by using the Akaike information criteria. Results were reproduced in three independent batches of prepared grana membranes.

Figure 2. HS-AFM characterization of the protein mobility observed in the first group of membranes. (**A**) Time-average image of a representative HS-AFM movie. Each image was acquired at 1 frame per second and averaged over 50 frames. (**B**) Mean square displacement (MSD) trajectories of 53 proteins; gray thin lines are MSD trajectories of each tracked protein in this membrane, and the superimposed black thick line is the average trajectory of all proteins selected in this grana membrane. The confined diffusion model agrees well with the average displacement of proteins in the first group of membranes.

Figure 3. HS-AFM characterization of the protein mobility observed in the second group of membranes. (**A**) Time-lapse HS-AFM images showing the heterogeneous protein mobility in the second group of membranes. Images were acquired at 1 frame per second. Corresponding illustrations of few proteins enclosed in the red squares are presented to facilitate the visualization of the protein dynamics. The particles in the cartoon were drawn freehand by visually tracing the protein's contour in the HS-AFM images. Z-scale, 6.7 nm. (**B**) MSD trajectories of the proteins selected in this membrane (N = 50). Gray lines are individual proteins' MSD trajectories; superimposed yellow line is the MSD average of all proteins; dashed black line is a fit to a confined diffusion model (Eq. 2); and orange dotted line is a fit to the Brownian diffusion model (Eq. 3). Inset: one AFM frame with eight MSD trajectories superimposed to their proteins. (**C**) Relationship between each protein's confined length and its initial diffusion coefficient (4 s). A protein's mobility can be segregated into two distinct groups as shown in blue circles and magenta squares, according to the k-means criteria. (**D**) Average MSD traces of two distinct groups (blue and magenta in C); dotted and dashed lines are the fits to Brownian and confined diffusion models, respectively.

Figure 4. HS-AFM characterization of the rotational displacement of a dimeric structure. (**A**) Time-lapse HS-AFM images illustrating the rotation of a dimeric protein (magenta arrow) with respect to its neighbor protein (blue arrow) captured at 1 fps. Corresponding illustrations are shown in the right (the particles were drawn by following the protein's contour as described in Fig. 3). Z-scale, 4.5 nm. (**B**) Variation of the angle (θ) in panel A over 50 s.

bioRxiv preprint doi: https://doi.org/10.1101/426759; this version posted September 27, 2018. The copyright holder for this preprint (which was not certified by peer review) is the author/funder, who has granted bioRxiv a license to display the preprint in perpetuity. It is made available under aCC-BY-NC-ND 4.0 International license.

(**C**) Time-course examples of the 2D correlation coefficient of variation (CCV) for two different proteins. Non-rotational symmetry will produce CCV values closer to 1. Rotational displacement is depicted by the red trace. Negligible rotational displacement is illustrated by the blue trace (blue arrow in the bottom right inset). (**D**) Left, the average HS-AFM image. Right, height profiles indicated in averaged AFM images (left).